Ultrasonics 94 (2019) 319–331

Contents lists available at ScienceDirect

Ultrasonics

journal homepage: www.elsevier.com/locate/ultras

Multi-mode reverse time migration damage imaging using ultrasonic guided waves

Jiaze He[a,b,*], Cara A.C. Leckey[c], Patrick E. Leser[c], William P. Leser[c]

[a] National Institute of Aerospace, Hampton, VA 23666, USA
[b] North Carolina State University, Raleigh, NC 27695, USA
[c] NASA Langley Research Center, Hampton, VA 23618, USA

ARTICLE INFO

Keywords:
Multi-mode
Guided waves
Damage imaging
Reverse-time migration
Elastodynamic finite integration technique

ABSTRACT

The sensitivity of Lamb wave modes to a particular defect or instance of damage is dependent on various factors (e.g., the local strain energy density due to that wave mode). As a result, different modes will be more useful than others for damage detection and quantification, dependent on damage type and location. For example, prior work in the field has shown that out-of-plane modes may have a higher sensitivity than in-plane modes to surface defects in plates. The excitability of a certain data acquisition system and the corresponding resolution for damage imaging also varies with frequency. The aim of the present work was to develop a multi-mode damage imaging technique that enables characterization of damage type and size, general sensitivity to unknown damage types, higher resolution imaging, and detectability regardless of the data acquisition system used. A reverse-time migration (RTM) imaging algorithm was combined with a numerical simulator—the three-dimensional (3D) elastodynamic finite integration technique (EFIT)—to provide multi-mode damage imaging. The approach was applied to two simulated case studies featuring damaged isotropic plates. Sensitivities of damage type to wave mode were investigated by separating the A_0 and S_0 Lamb wave modes obtained from the resultant RTM wavefields.

1. Introduction

Ultrasonic guided waves enable long distance nondestructive evaluation (NDE) and structural health monitoring (SHM) of plate-like structures. Depending on excitation frequency and plate thickness, various wave modes can exist, each with different phase and group velocities. The number of modes increases with frequency to infinity. These mode variations complicate the detection and quantification of damage as they lead to wave dispersion and create complex scattering patterns. Furthermore, mode conversion complexity, which increases with the number of modes, must be considered when Lamb waves reflect at structural boundaries [1], or interact with plate thickness variation [2], adhesive joints [3], or delaminations [4]. The most common approach to minimizing the above challenges is to excite only single-mode Lamb waves through careful transducer design and excitation signal selection [5–7]. This approach inherently restricts the range of available excitation frequencies.

Despite the associated difficulties of data processing for multiple wave modes, higher frequency ranges, and thus multiple wave modes, can enable the following damage detection advantages. Higher frequencies correspond to smaller wavelengths, which improves resolution for damage imaging [8]. Excitability varies for certain data acquisition systems at different frequencies [9–12], which means that the operating frequency range varies with hardware. Multi-mode imaging alleviates restrictions on frequency range, thus enabling the use of a system's optimal frequency. The sensitivity to anomalies is also different at various frequencies due to the "steepness" variation in the dispersion curves [13,10,14] such that multi-mode imaging enables use of the frequency that is most sensitive to the damage type of interest. By taking advantage of the sensitivity of various modes to different damage types (e.g., thickness loss or delamination) and accounting for mode conversion, damage types can possibly be identified in addition to simultaneous damage localization and sizing.

Foundational research into multi-mode damage detection has been conducted in an attempt to realize these benefits. Multi-mode total focusing method (TFM) considers longitudinal and shear waves by considering multi-paths including transmission, reflection, and mode conversions [15,16]. Plane waves were also used for multimodal ima-

* Corresponding author at: National Institute of Aerospace, Hampton, VA 23666, USA.
E-mail addresses: jiaze.he@nianet.org, jhe7@ncsu.edu (J. He).

https://doi.org/10.1016/j.ultras.2018.08.005
Received 2 June 2018; Received in revised form 5 August 2018; Accepted 12 August 2018
Available online 24 August 2018

ging [17]. Filtering can be done to reduce the artifacts of the images due to non-physical modes [18,19].

Theoretical formulations were derived by Kamal et al. [20] and Chen et al. [21] to better understand and enable convenient usage of multi-mode Lamb waves generated by piezoelectric wafer active sensors (PWAS). Ren and Lissenden developed Polyvinylidene fluoride (PVDF) multi-element Lamb wave sensors to improve reception of multi-mode signals [22]. Leckey et al. implemented the three-dimensional (3D) elastodynamic finite integration technique (EFIT) for multi-mode Lamb wave scattering simulation in both isotropic structures [23] and composites [24], which has also been used as a tool to study wavefield analysis and wavefield imaging [25,26]. Huthwaite et al. studied Lamb wave mode selection for tomography with the influence of coating on a cylindrical tube [27]. Philtron and Rose [28] developed a mode perturbation method to identify the optimal Lamb wave modes using quantifiable wave characteristics. With these advancements, multi-mode Lamb wave-based damage imaging has become more feasible, but is still largely unexplored.

Chan, Rose and Wang [29] generalized the theory of single-mode diffraction tomography (DT), a commonly used imaging technique, to a multi-mode theory and implemented A_0-mode DT to study scattering effects and the effect of noise. Wave propagation in complex structures can be modeled using finite element analysis (FEA) ([30,31]) and semi-analytical finite element (SAFE) ([32,33]). Advancements in computational technologies (e.g., general-purpose computing on graphical processing units (GPUs) [34,35]) have enabled the use of these methods to realize high-resolution imaging methods such as reverse time migration (RTM) [36,37] and full waveform inversion (FWI) [38,39] for complex structures. RTM was originally developed for the field of geophysics [40,41] but has also been successfully used for guided wave-based damage imaging [42–44]. He and Yuan implemented a 2D limited-view scan with RTM using a normalized zero-lag cross-correlation (NZLCC) imaging condition for both isotropic plates [45] and composites [37] in which the resulting images represented the reflection coefficient of the damage. However, RTM as a quantitative damage evaluation method has not yet been studied for multi-mode guided-wave imaging applications.

The aim of the present work is to develop a multi-mode imaging technique using RTM that will allow for identification of damage size and location, and, potentially, damage type. To do this, a simulation tool must be available for back-propagation that can model the wave dynamics in the structure of interest. Here, it is proposed to use RTM in concert with the numerical simulation algorithm, EFIT, for multi-mode damage imaging. With this combination, EFIT generates wavefields that allow for wave mode separation. The combination with RTM is expected to address mode conversion effects for damage reflection, since all acquired wave modes are used for imaging.

The proposed technique requires data acquisition devices that can measure the x, y, and z components of the wavefield at an array of locations. Ideally, a 3D laser Doppler vibrometer (LDV) would be used for this task. In this work, however, access to a 3D LDV with an appropriate frequency range for multi-mode imaging was not available. Instead, EFIT was used to simulate experiments, meaning that both the excitation via piezoelectric wafer and data collection of damage-scattered signals at the array locations via a 3D LDV were simulated with EFIT.

The remainder of this paper is organized as follows. First, the necessary background information will be briefly presented; this includes an introduction to single-mode RTM and wavefield analysis. The next section presents derivation of the theory of multi-axis, multi-mode RTM, developed from single mode RTM theory, and introduces the numerical simulator EFIT. Finally, the method is demonstrated numerically through the simulation of a half-thickness notch and a middle-plane disbond. For both cases, A_0 and S_0 Lamb wave modes were considered. Damage images were obtained using a variety of different imaging conditions, frequencies, and modes as part of the study.

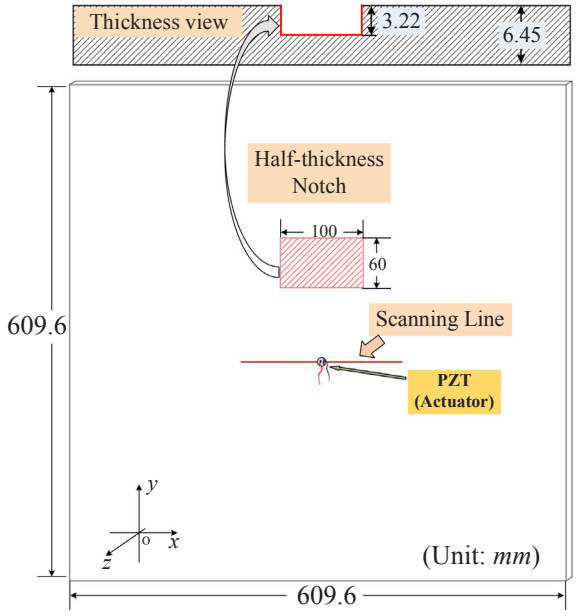

Fig. 1. Illustration of the plate and the sensor array for the half-thickness notch (HTN) damage.

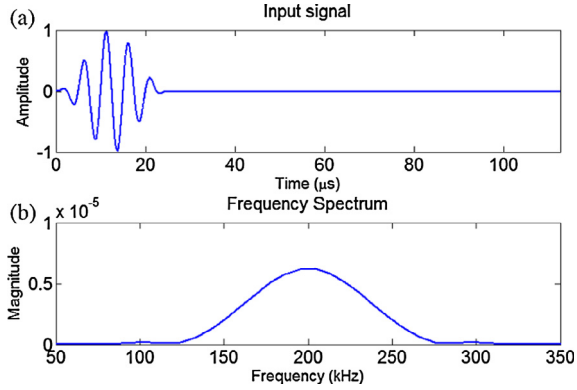

Fig. 2. Excitation signal in (a) the time domain (b) the frequency domain.

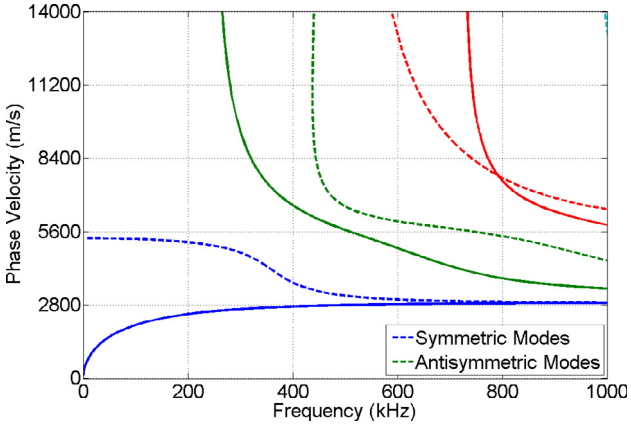

Fig. 3. Dispersion relation between frequency and phase velocity.

2. Methodology review: reverse-time migration (RTM) and multi-mode separation techniques

2.1. Notation

t-s domain	time - space domain
f-s domain	frequency - space domain
f-k domain	frequency - wavenumber domain
k_x-k_y domain	2-D wavenumber domain with respect to a single frequency or time
$u(x, y, t)$	Total wavefield in the *t-s* domain
$u_+(x, y, t)$	Single-mode forward wavefield (FW) in the *t-s* domain
$u_-(x, y, t)$	Single-mode backward wavefield (BW) in the *t-s* domain
$\overline{U}(x, y, \omega)$	Total wavefield in the *f-s* domain
$U(k_x, k_y, \omega)$	Total wavefield in the *f-k* domain
$\mathscr{F}_{3D}$	3-D FFT, e.g. $U(k_x, k_y, \omega) = \mathscr{F}_{3D}(u(x, y, t))$
$\mathscr{F}_{3D}^{-1}$	Inverse 3-D FFT, e.g. $u(x, y, t) = \mathscr{F}_{3D}^{-1}(U(k_x, k_y, \omega))$
$U_+(k_x, k_y, \omega)$	Single-mode forward wavefield in the *f-k* domain
$U_-(k_x, k_y, \omega)$	Single-mode backward wavefield in the *f-k* domain
$\mathscr{F}_{1D}$	1-D FFT, e.g. $U_{xy}(x, y, \omega) = \mathscr{F}_{1D}(u(x, y, t))$
$u_+^\alpha(x, y, t)$.	$\alpha = x, y, z$. When $\alpha = z$, it denotes the *z*-components of the FW in the *t-s* domain
$U_-^\alpha(k_x, k_y, \omega)$	$\alpha = x, y, z$. When $\alpha = y$, it denotes the *y*-components of the BW in the *f-k* domain
$U_{+\beta}^\alpha(k_x, k_y, \omega)$	filtered single-mode ($\beta = A_0$ or S_0) from the *f-k* domain FW
$U_{-\gamma}^\alpha(k_x, k_y, \omega)$	filtered single-mode ($\gamma = A_0$ or S_0) from the *f-k* domain BW
$\overline{U}_{+\beta}^\alpha(x, y, \omega)$	filtered single-mode ($\beta = A_0$ or S_0) from the *f-s* domain FW
$\overline{U}_{-\gamma}^{\alpha\,*}(x, y, \omega)$	filtered single-mode ($\gamma = A_0$ or S_0) from the *f-s* domain BW

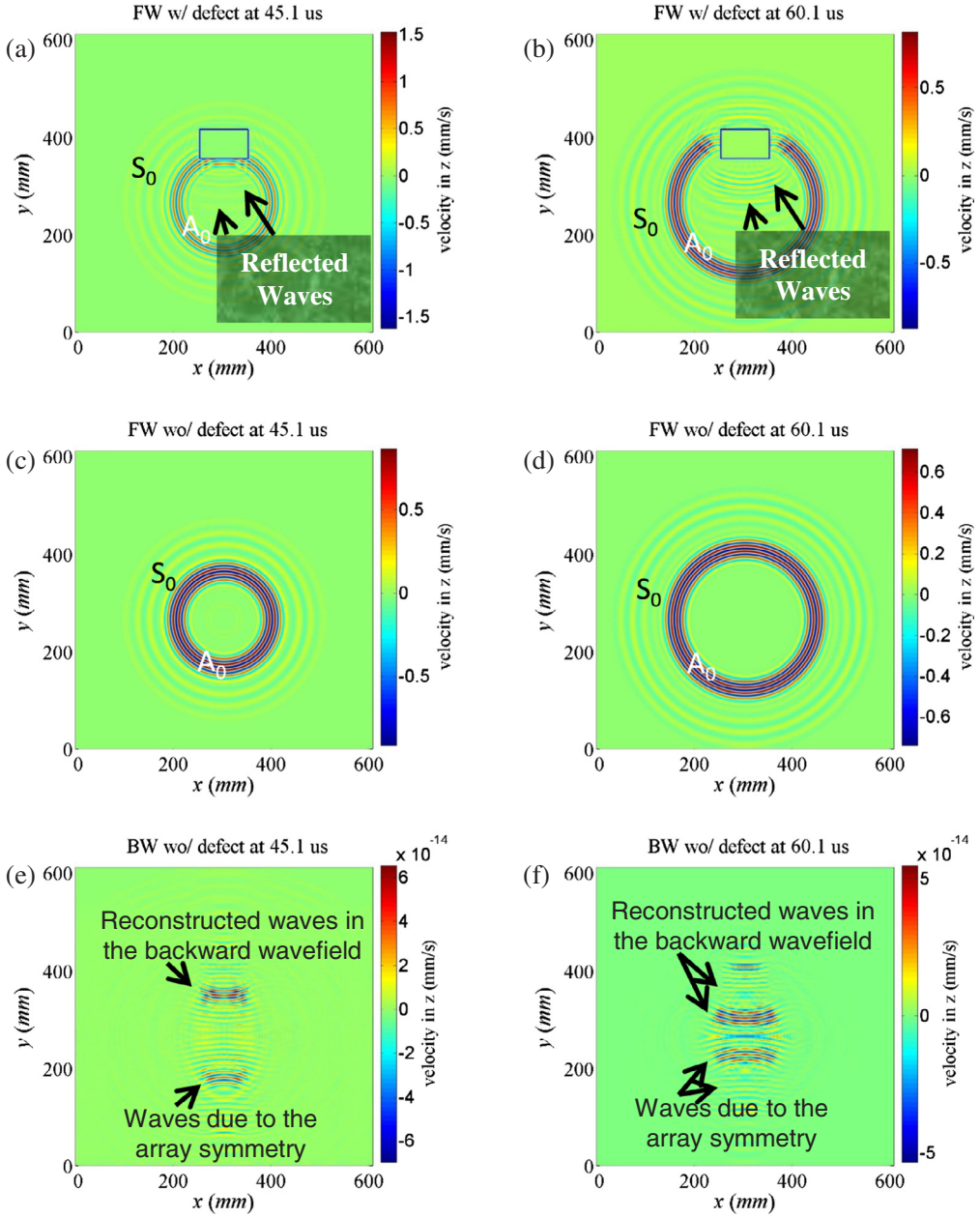

Fig. 4. Out-of-plane ($\alpha = z$) wavefield snapshots at time 45.1μs and 60.1μs for (a–b) the forward wavefield (FW) for the HTN case to generate damage scattered waves using EFIT, (c–d) the FW for the undamaged plate ($u_+^z(x, y, t)$) for data processing and imaging, and (e–f) the backward wavefield (BW) $u_-^z(x, y, t)$ in RTM.

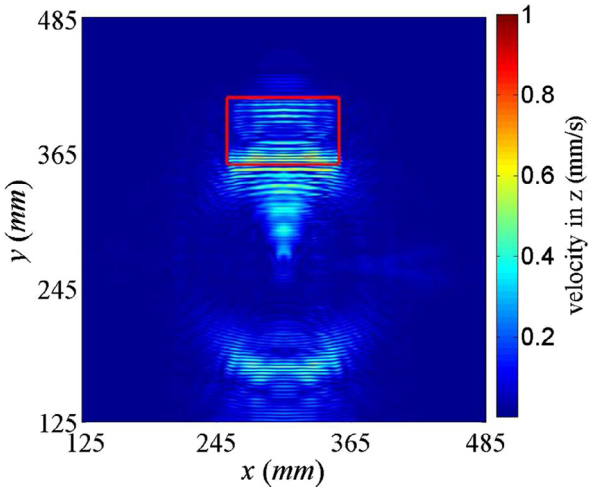

Fig. 5. Time-domain NZLCC ($I^{z}_{\mathrm{NZLCC}}(x, y)$) for all modes using v_z for the HTN (outlined by the red box). (For interpretation of the references to color in this figure legend, the reader is referred to the web version of this article.)

2.2. Principles of single-mode RTM

Only A_0-mode Lamb waves have been used in previous guided wave-based RTM research ([43,46,42,37]). In RTM, a single actuator serves as a source to generate a forward wavefield, and sensors at designated locations receive the waves scattered by the damage. Time-domain RTM has three steps: (i) the forward-time extrapolation from the actuator, (ii) the extrapolation of the time-reversed scattered wavefield received at the sensor array, and (iii) the application of imaging conditions. Details of the three steps are included in [45]. The wavefields generated in the first and second steps will be referred to as the forward wavefield (FW) and backward wavefield (BW), respectively, where both FW and BW are numerically generated wavefields with the pristine structure as the background media. Not only is the arrival time for both the time-reversed backward wavefield and the forward wavefield the same at the damage boundaries, but the two wavefields are also exactly in-phase at these boundaries. As a result, the zero-lag cross-correlation (ZLCC) between the forward and backward wavefield results in large values at damaged regions and low values elsewhere. These values then form an image when displayed as intensities.

The ZLCC imaging condition uses all the frequency content to calculate the value for each location (x, y) on the image. Mathematically, the image value for grid point (x, y) is defined as:

$$I_{\mathrm{ZLCC}}(x, y) = \int_0^T u_+(x, y, \tau) u_-(x, y, T-\tau) d\tau. \tag{1}$$

where $u_+(x, y, t)$ is the forward wavefield, $u_-(x, y, t)$ is the backward wavefield, and T is the time duration in a single migration experiment. The single-mode ZLCC imaging condition can also be implemented in the frequency-space (f-s) domain for a single frequency [43],

$$\overline{I}^{\omega}_{\mathrm{ZLCC}}(x, y, \omega) = \overline{U}_+(x, y, \omega)\overline{U}^*_-(x, y, \omega), \tag{2}$$

where '$*$' represents the complex conjugate.

An improved ZLCC imaging condition can include the normalization terms of u_+ in the denominator, which takes into account the amplitude change caused by attenuation due to geometrical spreading or dispersion. This is referred to as the normalized ZLCC (NZLCC) imaging condition ([45,37]), which is expressed as

$$I_{\mathrm{NZLCC}}(x, y) = \frac{\int_0^T u_+(x, y, \tau) u_-(x, y, T-\tau) d\tau}{\int_0^T u_+^2(x, y, \tau) d\tau}. \tag{3}$$

The resulting image represents the spatial variation of the reflective coefficient or the "reflectivity" [37]. Due to the frequency-dependence of reflectivity, it can be used for estimating damage severity using the dispersion relation [47].

2.3. Wavemode separation in frequency-wavenumber (f-k) domain

The most general approach to identify and separate various wave modes is wavefield analysis. Ruzzene ([48]) proposed a frequency-wavenumber (f-k) domain filtering technique to separate back-scattered waves (i.e., reflections of the incident waves caused by damage) using wavefield analysis. The total time–space (t-s) domain wavefield $u(x, y, t)$ was transformed to the f-k space domain using the 3D fast Fourier transform (FFT),

$$U(k_x, k_y, \omega) = \mathscr{F}_{3D}(u(x, y, t)), \tag{4}$$

where $U(k_x, k_y, \omega)$ represents the total wavefield in the f-k domain.

Since the incident waves and the back-scattered waves propagate in different directions, their wave vectors dictate different wave propagation directions in the wavenumber (k_x-k_y) domain. Hence, the incident waves and reflected waves can be separated in this domain. If material properties are known, it is possible to design filters for different wave modes using the wave dispersion relationship and a raised-cosine filter [49].

In this research, wave mode separation was performed in the k_x-k_y domain within the frequency range of interest. The wavefield filters used were designed based on the mode distribution in the k_x-k_y domain at the each frequency. More details about the filters can be found in Section 3.3.

3. Multi-mode reverse-time migration

The main contribution of this paper is the development of RTM theory for multi-mode damage imaging. In this section, the major challenges faced are addressed first, followed by a discussion of EFIT and its utility for multi-mode imaging. These subsections are followed by the presentation of multi-mode RTM imaging conditions for all wave modes and multiple separated wave modes, respectively.

3.1. Separation of multi-mode waves

The wavefield analysis and filtering techniques summarized in the Section 2.2 require the collection of full wavefield data. However, sensor arrays used in practice, such as those described in Section 1, typically do not acquire data at enough locations to preserve the spatial information of the full wavefield. As a result, commonly used arrays cannot differentiate between wave modes of the received signals. Thus, associating those signals with correct wave physics (e.g., group velocity) for imaging is rather challenging. For traditional array-based imaging, this issue is usually avoided by assuming the existence of a single dominant mode. As stated previously, this assumption limits the resolution, undermines damage detectability, and discards useful information relevant to determining damage types.

On the other hand, in RTM, the back-propagation of the time-reversed scattered signals from the sensor locations creates a backward wavefield that reconstructs the scattered wavefield, especially in the vicinity of the damage boundaries. Based on this fact, mode separation using the wavefield filtering techniques is potentially applicable to the backward wavefield, if the wave propagator has the capability of modeling multi-mode waves.

3.2. Simulating wave propagation for multi-mode imaging

3.2.1. Imaging using single-mode waves

For past research on single-mode RTM [42–44], the back-propagation used only the total received signals as the out-of-plane components of the received A_0 waves for reconstruction. This implementation is

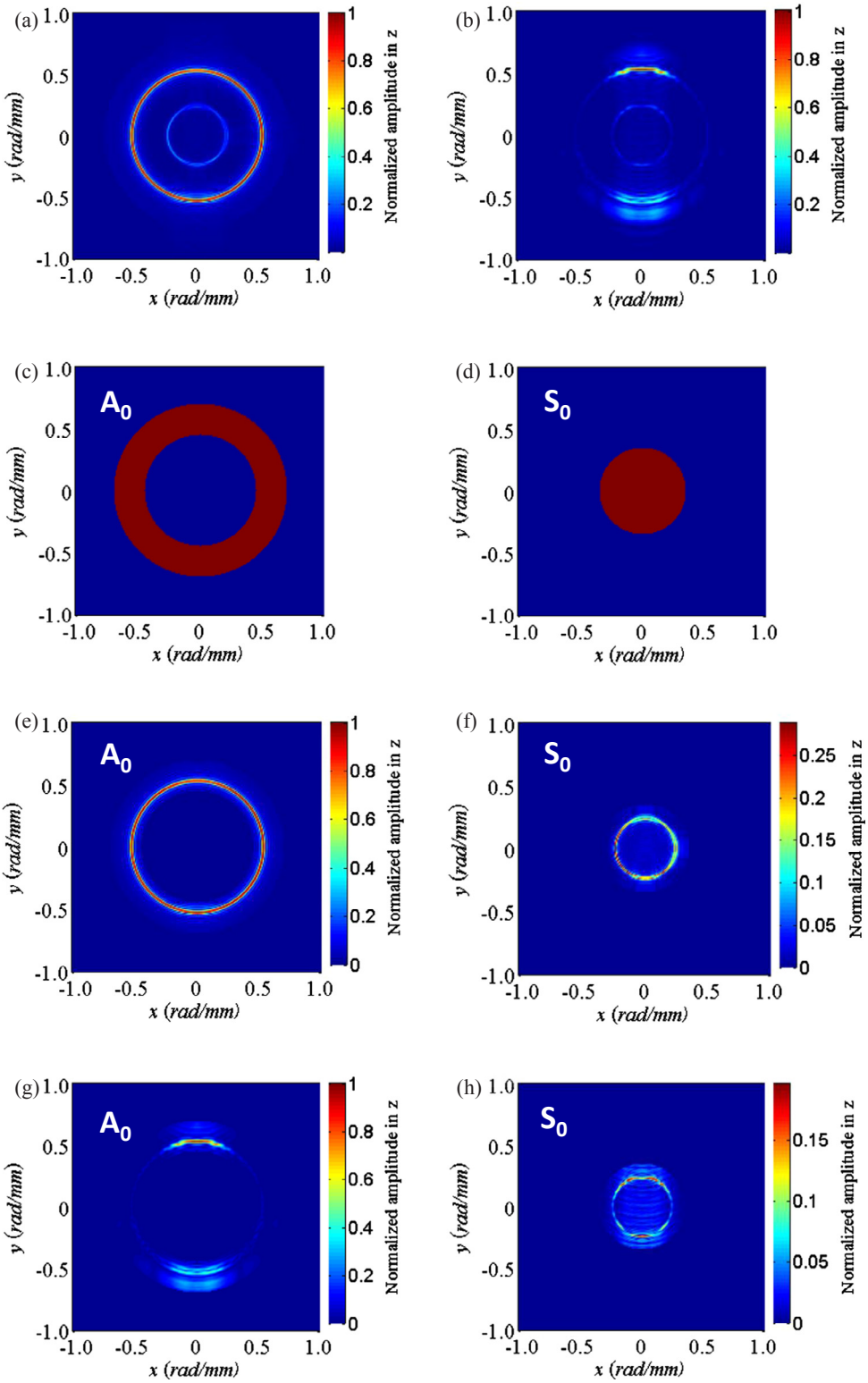

Fig. 6. *f*.-*k* filtering for the total wavefields, $U^z_+(k_x, k_y, \omega)$ and $U^z_-(k_x, k_y, \omega)$ at 201 kHz for the HTN case. (a) $U^z_+(k_x, k_y, \omega)$; (b) $U^z_-(k_x, k_y, \omega)$;k_x-k_y filters for (c) A_0 mode and (d) S_0 mode; filtered FW of (e) A_0 mode ($U^z_{+A0}(k_x, k_y, \omega)$) and (f) S_0 mode ($U^z_{+S0}(k_x, k_y, \omega)$); and filtered BW of (g) A_0 mode ($U^z_{-A0}(k_x, k_y, \omega)$) and (h) S_0 mode ($U^z_{-S0}(k_x, k_y, \omega)$).

based on an approximation that the dominant components of single-mode A_0 waves are in the out-of-plane direction. The implementation was incomplete due to the missing in-plane components of the waves. Furthermore, when dealing with both A_0 and S_0 wave modes for RTM, the in-plane components for symmetric modes (e.g., S_0 mode), cannot be discarded. Additionally, for 2-D acoustic models [38,39,50], it is extremely difficult to calculate the propagation of all wave modes within a single simulation. Therefore, manually identifying target modes before imaging in order to process multi-mode data is typically required. As a result, mode conversion can be difficult to address. To overcome this challenge, a numerical simulator that can handle multi-mode wave propagation is needed for multi-mode RTM.

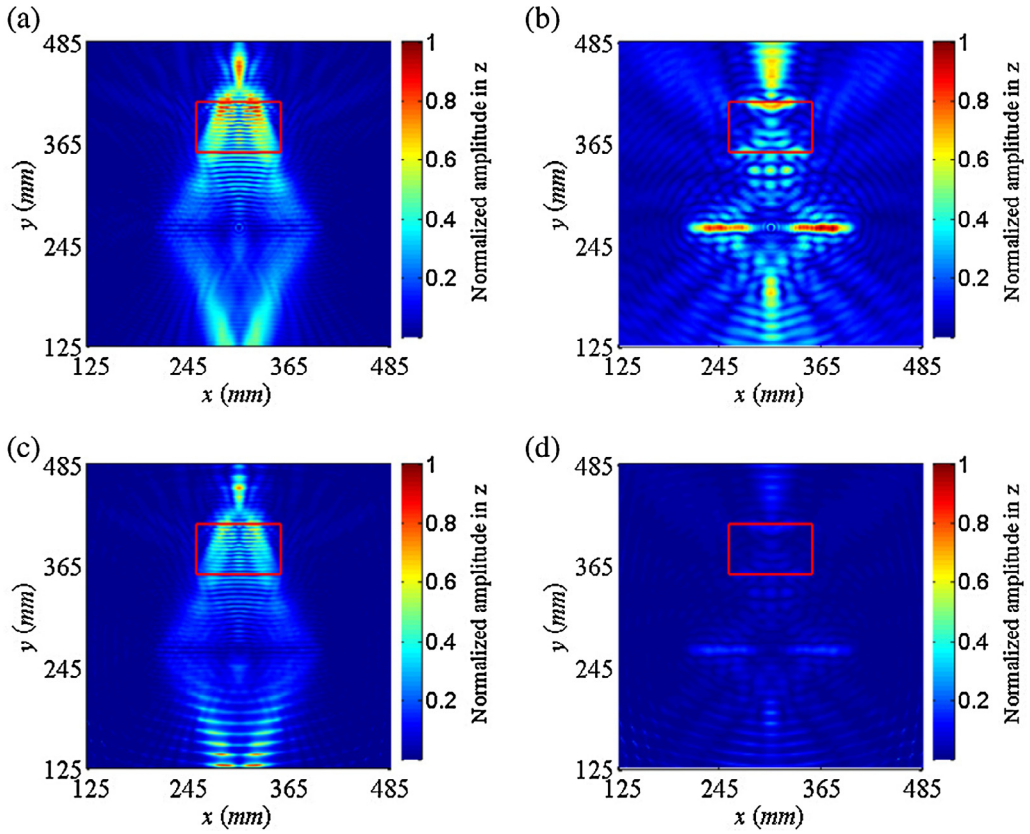

Fig. 7. Multi-mode NZLCC in the *f-k* domain at 201 kHz using v_z for the HTN (outlined by the red box). Images shown are from FW-BW mode pairs (a) A_0-A_0, (b) A_0-S_0, (c) S_0-A_0, and (d) S_0-S_0. (For interpretation of the references to color in this figure legend, the reader is referred to the web version of this article.)

3.2.2. EFIT-based imaging using multi-mode waves

In this study, EFIT was used to calculate the Lamb wave propagation for RTM. EFIT is a standard staggered-grid, finite difference, explicit time-domain approach for calculating elastodynamic motion in solid media ([51]). The mathematical approach leads to straight-forward algebraic equations that are readily implemented in any programming language. Additionally, the equations can be parallelized to run on multi-core, cluster, or many-core computational hardware to achieve faster computational speeds. The EFIT simulations implemented in this work are 3D in space, explicit in time, and correspond to a cubic Cartesian numerical grid. The x, y, and z axes are defined in Section 4. All three velocity components, in-plane (v_x, v_y) and out-of-plane (v_z), and all shear (σ_{xy}, σ_{xy}, σ_{yz}) and normal (σ_{xx}, σ_{yy}, σ_{zz}) stress components are calculated at every spatial grid cell, at each time step.

Using EFIT with RTM, separating different modes at the sensors was not required. All x, y, and z velocity components of the damage-scattered signals were simultaneously back-extrapolated to obtain the wavefields. Since the wavefields become viable, mode separation techniques based on wavefield analysis become applicable as well.

3.3. RTM imaging conditions for all wave modes

In EFIT, the 3D velocity wavefield is accessible at all nodes in the model. In this paper, all wavefields and signals are always obtained from velocities in the x, y, and z directions and are from the front surface of the plate (the surface shown in the top view of Figs. 1 and 9) only. For instance, the z-component of the forward velocity wavefield on the front surface in the *t-s* domain is denoted as $u_+^z(x, y, t)$ and the corresponding *f-k* domain wavefield is $U_+^z(k_x, k_y, \omega)$. Eq. (3) can then be rewritten as

$$I^{\alpha}_{\mathrm{NZLCC}}(x, y) = \frac{\int_0^T u_+^{\alpha}(x, y, \tau) u_-^{\alpha}(x, y, T-\tau) d\tau}{\int_0^T u_+^{\alpha 2}(x, y, \tau) d\tau}, \tag{5}$$

where $\alpha = x, y, z$. The forward wavefield calculated by EFIT contains all wave modes at the input frequency ranges.

Due to mode conversion effects at a damage region, A_0 waves lead to A_0 and S_0 scattered waves. Similarly, S_0 mode waves can also generate A_0 and S_0 damage-scattered waves. For instance, assuming a certain damage type, forward A_0 waves generate both A_0 mode and S_0 mode reflections, while S_0 mode waves only cause scattered S_0 waves. This particular mode conversion case will be referred to as Case A. The above imaging conditions account for the contributions from all modes for all frequencies along each axis.

In RTM, a backward wavefield reconstructs the damage-reflected wavefield. Imaging conditions use a pair of single-mode wavefields for imaging, one from the forward wavefield and the other from the backward wavefield. The images created using Eq. (5) would include all of the reflections described above. However, inevitably, the images will contain artifacts from reflected S_0 waves with forward A_0 waves, if we take the aforementioned Case A as an example. Since the location of the damage is not known *a priori*, eliminating those artifacts is difficult. These added challenges are offset by the potential benefits of multi-mode imaging, which include a wider selection of frequencies for improved data acquisition system performance and the ability to simultaneously characterize damage size, location, and type. Examples of the proposed imaging condition can be found in Section 4.

3.4. RTM imaging conditions for multiple separated wave modes

Detailed information on which mode pair contributes the most to

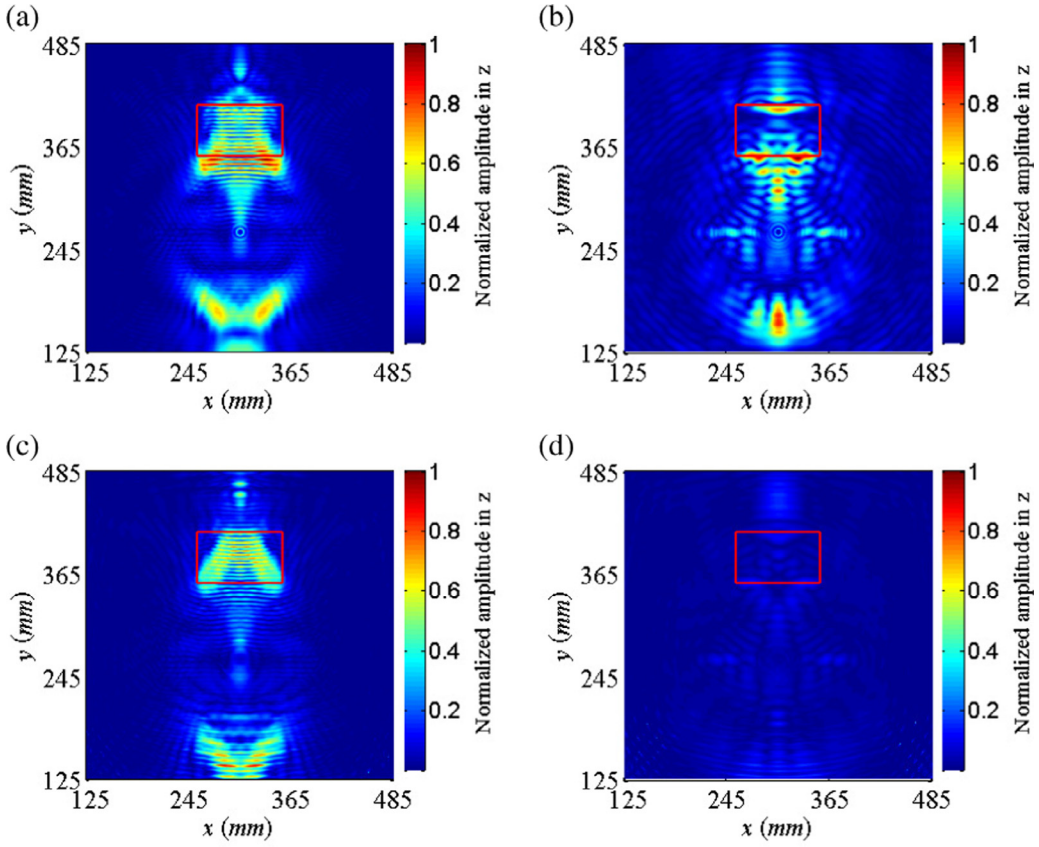

Fig. 8. Stacked multi-mode, *f-k* domain NZLCC within a frequency range of 183–228 kHz using v_z for the HTN (outlined by the red box). Images from mode pairs (a) A_0-A_0, (b) A_0-S_0, (c) S_0-A_0, and (d) S_0-S_0. (For interpretation of the references to color in this figure legend, the reader is referred to the web version of this article.)

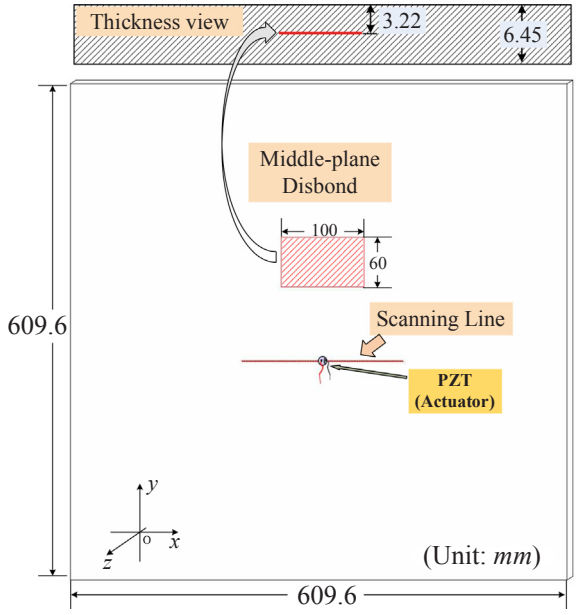

Fig. 9. Illustration of the plate and the sensor array for the mid-plane disbond (MPD) damage.

the final damage image can be obtained through *f-k* analysis. As stated in Section 2.3, 3D FFT converts the *t-s* domain signals into the *f-k* domain. Using Eq. (4), the forward wavefield $u_+^\alpha(x, y, t)$ and the backward wavefield $u_-^\alpha(x, y, t)$ are converted to $U_+^\alpha(k_x, k_y, \omega)$ and $U_-^\alpha(k_x, k_y, \omega)$ in the *f-k* domain for each axis,

$$U_+^\alpha(k_x, k_y, \omega) = \mathscr{F}_{3D}(u_+^\alpha(x, y, t)), \tag{6a}$$

$$U_-^\alpha(k_x, k_y, \omega) = \mathscr{F}_{3D}(u_-^\alpha(x, y, t)). \tag{6b}$$

To seperate different wave modes, multi-mode wavenumber bandpass filters are needed. One example, borrowed from [52] is

$$W(k_x, k_y, \omega) = \begin{cases} 0, & |\boldsymbol{k}| < k_1 \\ 1, & k_1 \leqslant |\boldsymbol{k}| \leqslant k_2, \\ 0, & |\boldsymbol{k}| > k_2 \end{cases} \tag{7}$$

where low and high wavenumber bandpass cutoffs are denoted as k_1 and k_2, $\mathbf{k} = [k_x, k_y]^T$, and, || denotes the L_2 norm. More comprehensive, smoothed filters, such as those introduced in [49], can also be used.

For compactness, the wave modes in the forward wavefield will be denoted as β ($\beta = A_0$ or S_0), and the wave modes in the backward wavefield will be referred to as γ ($\gamma = A_0$ or S_0). The single-mode wavefield separated from U_+^α and U_-^α are defined using Eqs. (6) and Eqs. (7),

$$U_{+\beta}^\alpha(k_x, k_y, \omega) = W_\beta(k_x, k_y, \omega) U_+^\alpha(k_x, k_y, \omega), \tag{8a}$$

$$U_{-\gamma}^\alpha(k_x, k_y, \omega) = W_\gamma(k_x, k_y, \omega) U_-^\alpha(k_x, k_y, \omega). \tag{8b}$$

where $\alpha = x, y, z; \beta = A_0$ or S_0; and $\gamma = A_0$ or S_0.

Applying 2D inverse FFT (IFFT) to $U_{+\beta}^\alpha$ and $U_{-\gamma}^\alpha$ at each frequency, the resulting single-mode wavefields in the *f-s* domain are obtained as $\overline{U}_{+\beta}^\alpha(x, y, \omega)$ and $\overline{U}_{-\gamma}^\alpha(x, y, \omega)$.

The above expressions are extended to a multi-axis, multi-mode ZLCC imaging condition for a single frequency,

$$\overline{I}_{\mathrm{ZLCC}}^{\omega\alpha\ \beta-\gamma}(x, y, \omega) = \overline{U}_{+\beta}^\alpha(x, y, \omega) \overline{U}_{-\gamma}^{\alpha\,*}(x, y, \omega). \tag{9}$$

Then the multi-axis multi-mode NZLCC for a single frequency is defined as,

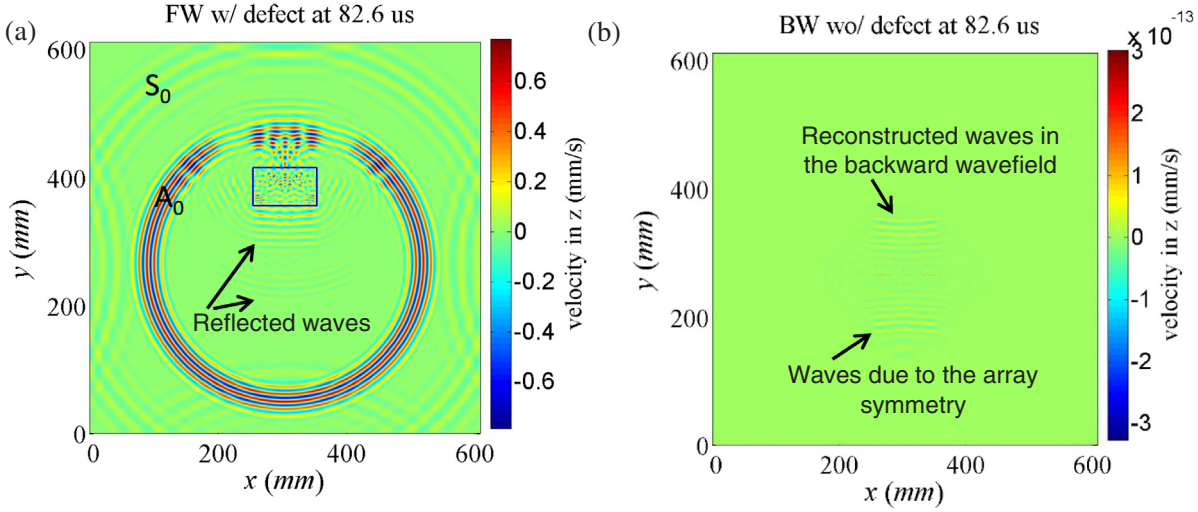

Fig. 10. Out-of-plane ($\alpha = z$) wavefield snapshots at time 82.6 μs of (a) the forward wavefield for damage scattered wave generation with the outlined MPD and (b) the backward wavefield $u_{-}^{z}(x, y, t)$ in RTM.

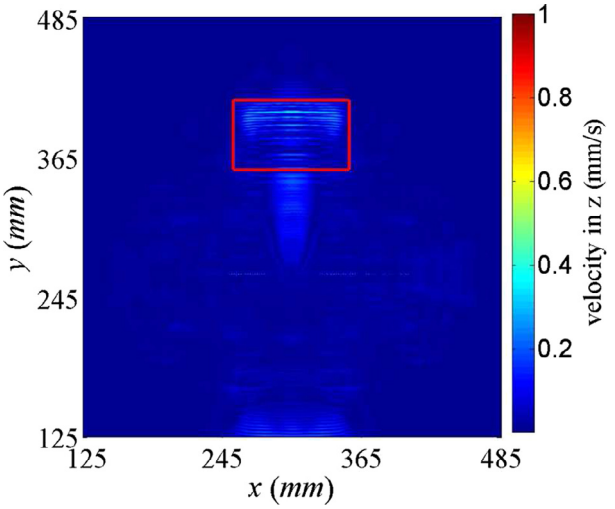

Fig. 11. Time-domain NZLCC for all modes using v_z for the MPD (outlined by the red box). (For interpretation of the references to color in this figure legend, the reader is referred to the web version of this article.)

$$\bar{I}^{\omega\alpha\ \beta-\gamma}_{\mathrm{NZLCC}}(x, y, \omega) = \frac{\bar{U}^{\alpha}_{+\beta}(x, y, \omega)\bar{U}^{\alpha\ *}_{-\gamma}(x, y, \omega)}{\bar{U}^{\alpha\ 2}_{+\beta}(x, y, \omega)}. \tag{10}$$

Finally, the total NZLCC image over the frequency band of interest for each mode pair ($\beta-\gamma$) in the corresponding axis (α) is obtained via the summation,

$$\bar{I}^{\alpha\ \beta-\gamma}_{\mathrm{NZLCC}}(x, y) = \sum_{\omega} \frac{\bar{U}^{\alpha}_{+\beta}(x, y, \omega)\bar{U}^{\alpha\ *}_{-\gamma}(x, y, \omega)}{\bar{U}^{\alpha\ 2}_{+\beta}(x, y, \omega)}. \tag{11}$$

4. Numerical simulation

The two primary goals of the numerical simulations were to test the effectiveness of the proposed multi-mode imaging conditions and to show the sensitivity of the approach to different damage types. The latter objective was achieved through imaging two distinct types of simulated damage (a notch and a mid-plane disbond) which had the exact same planform location and shape in an aluminum plate.

4.1. Simulation parameters

The isotropic form of the EFIT equations were used for the studies

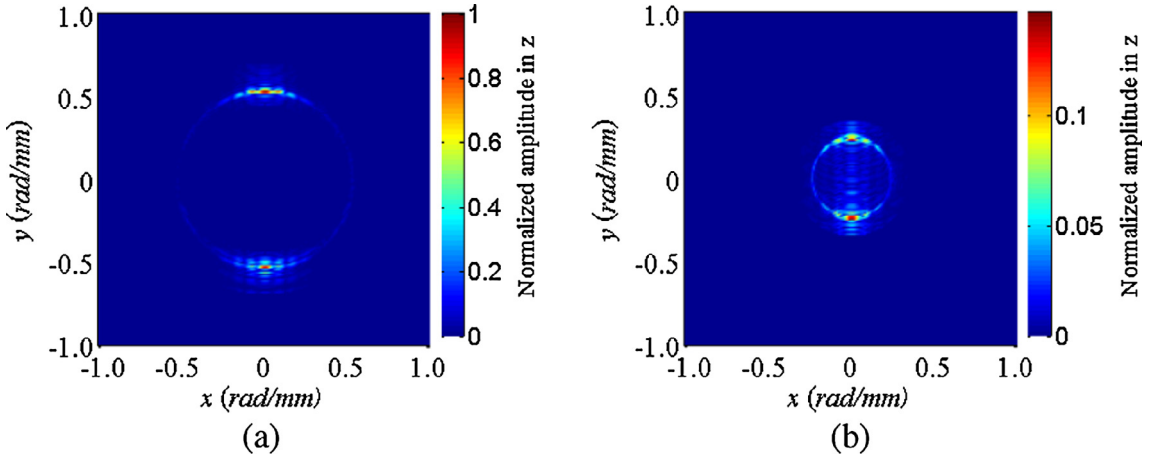

Fig. 12. *f*-*k* filtered backward wavefield $U_{-}^{z}(k_x, k_y, \omega)$ at 201 kHz for the k_x-k_y distribution in the MPD case for (a) A_0 mode ($U^{z}_{-A_0}(k_x, k_y, \omega)$) and (b) S_0 mode ($U^{z}_{-S_0}(k_x, k_y, \omega)$).

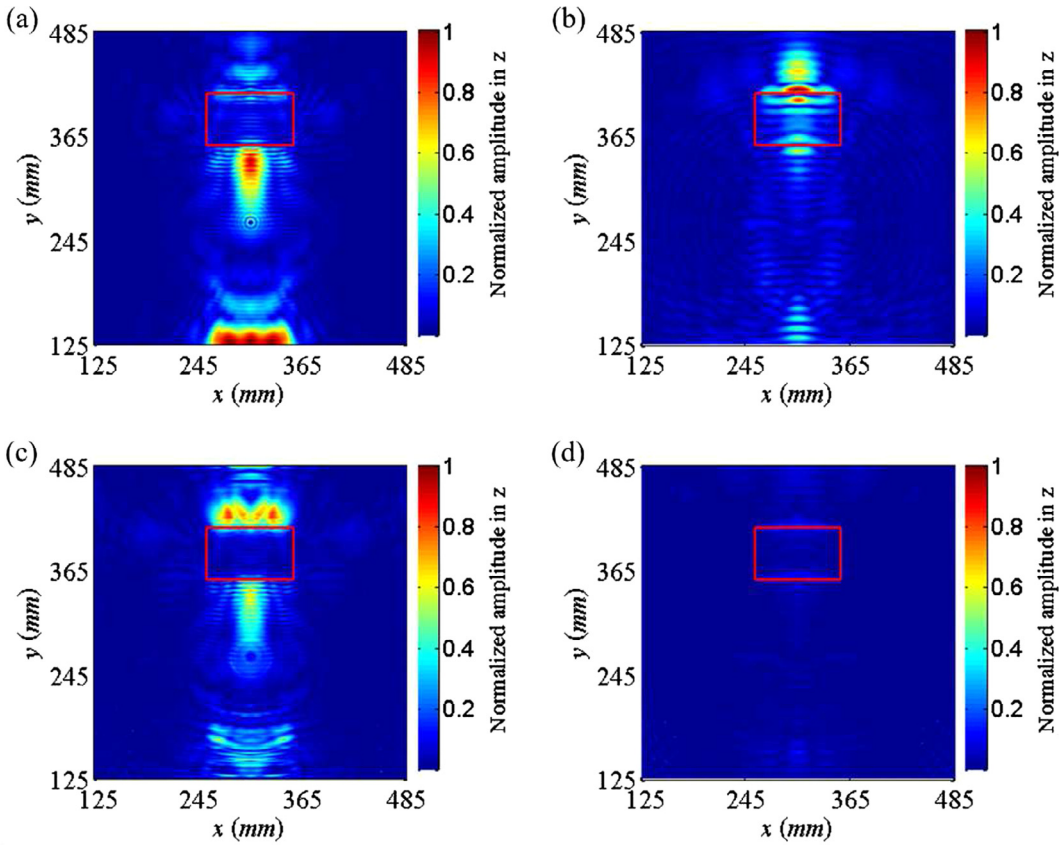

Fig. 13. Stacked multi-mode, *f-k* domain NZLCC for a frequency range of 183–228 kHz using v_z for the MPD (outlined by the red box). Images from mode pairs (a) A_0-A_0, (b) A_0-S_0, (c) S_0-A_0, and (d) S_0-S_0. (For interpretation of the references to color in this figure legend, the reader is referred to the web version of this article.)

Table 1
Comparison of MPD and HTN images using v_z.

V_z	A_0–A_0	A_0–S_0	S_0–A_0	S_0–S_0
HTN	✔	✖ ✔	✔	✖
MPD	✖	✖ ✔	✖	✖ ✔

presented here, as the material-of-interest was aluminum alloy 6061-T6. The overall simulated aluminum plate was 609.6 mm × 609.6 mm × 6.4 mm; i.e., the plate thickness (z-direction) was 6.4 mm. The plate density was 2780 kg m^{-3}. The first damage case is a rectangular half-thickness notch (HTN) with dimensions of 100 mm and 60 mm, shown in Fig. 1.

EFIT has specific spatial and time step requirements, as detailed in [51,23]. The spatial step size must satisfy $dx \leqslant \lambda_{min}/10$, where λ_{min} is the minimum wavelength in the simulation. For cases involving Lamb waves, dispersion curves should be assessed when selecting an appropriate value for λ_{min}. The time step must satisfy stability requirements (Courant-Friedrichs-Lewy (CFL) condition), which for the EFIT cubic numerical grid ($dx = dy = dz$) states that $dt \leqslant dx/(c_{max}\sqrt{3})$, where c_{max} is a constant dictated by stability constraints.

The excitation was a normal incidence 5-cycle Hann windowed sine wave with a center frequency of 200 kHz (Fig. 2). The simulations in this work used a spatial step size of $dx = 0.4$ mm and a time step size of $dt = 37.56$ ns. The spatial step size allowed for 16 grid points through the plate thickness. These step sizes satisfy the EFIT stability criteria and are based on a longitudinal speed of sound, c_{max}, of 6149 m/s and a minimum Lamb wave speed (based on dispersion curves), c_{min}, of 2400 m/s. The dispersion relationship is shown for this plate in Fig. 3. Only two fundamental modes (A_0 and S_0) exist at 200 kHz, at which the amplitude from both modes should be relatively large if a piezoelectric wafer is used [53].

As mentioned previously, the imaging techniques proposed in this research require data acquisition devices that can measure the x, y, and z components of the wavefield at an array of locations. A measurement device with this capability is the 3D LDV, which can be used to scan multiple locations, forming an array at which in-plane velocity (v_x and v_y) and out-of-plane velocity (v_z) are acquired as Lamb wave signals. Due to the lack of access to a 3D LDV with proper working frequencies, the measurement device was simulated in this research. The v_x, v_y and v_z at locations representing a linear array on the front surface of the plate were recorded in EFIT to simulate signals acquired by a 3D LDV. The scanning line shown in Fig. 1 was 200 mm long with a sensor spacing of 2 mm to avoid aliasing. The actuator was located at the center point of the linear array. The received signals at the linear array were recorded using the velocities in the x, y, and z axes to simulate experimental measurements, but the wavefields with damage were not used for imaging.

4.2. Imaging results using v_z for the half-thickness notch

This section demonstrates the imaging process using the v_z measurements on the surface of the plate (analogous to using a 1D LDV). The center of the HTN for this simulation was 120 mm away from the center of the actuator.

4.2.1. Wave propagation snapshots

Fig. 4(a–b) shows the forward wavefields from the HTN case at times 45.1 μs and 60.1 μs, respectively. This forward simulation was performed only for generating damage scattered signals and these wavefields containing damage scattered waves were not used for imaging. The reflected waves display different wavelengths, representing A_0 and S_0 damage-scattered waves. Fig. 4(c–d) illustrates the FW without damage at the same time steps, which were generated for the purposes of

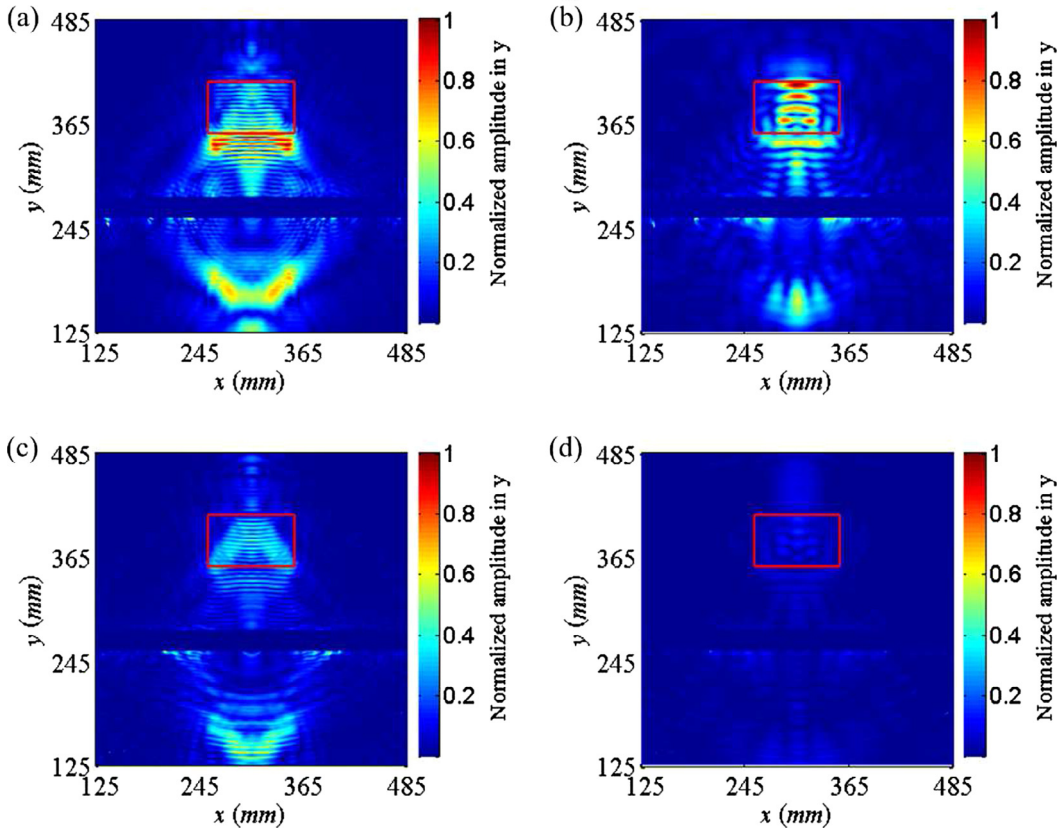

Fig. 14. Stacked multi-mode, *f-k* domain NZLCC for a frequency range 183–228 kHz using v_y for the HTN (outlined by the red box). Images from mode pairs (a) A_0-A_0, (b) A_0-S_0, (c) S_0-A_0, and (d) S_0-S_0. [Intensity values in the thin, constant-y, rectangular region that covers the array area were set to zero, to mitigate the artifacts caused by the small values of the denominator in Eq. (11) of this region.] (For interpretation of the references to color in this figure legend, the reader is referred to the web version of this article.)

data post-processing and imaging. In Fig. 4(e–f), the reconstructed waveforms of the reflected waves in (a–b) can be seen in the backward wavefield. Here the backward wavefield snapshots are illustrated in a time-reversed manner such that the time steps shown in (e–f) correspond to the exact same time steps in (a–d). From this figure, reflected A_0 waves are accurately reconstructed. In Fig. 4, similar wave packets also appear below the scanning line, which will generate artifacts commonly referred to as a "ghost image," as shown later in Fig. 5. This ghost image effect can be reduced through the use of 2D arrays [54,45].

Applying the imaging condition from Eq. (5), the total results for the time-domain NZLCC for all wave modes using v_z are shown in Fig. 5. The damage region is enclosed by the red rectangle. Despite the artifacts in front of the damaged area, the main region of the damage was successfully imaged. The results shown are mixtures of all incident and reflected mode pairs.

4.2.2. Multi-mode wave separation

To extract more information on the contribution of each mode pair, the generated FW and BW are processed with the wavefield analysis techniques of Section 2.3. Using Eq. (6), $u_+^z(x, y, t)$ and $u_-^z(x, y, t)$ were converted to the *f-k* domain (wavefields $U_+^z(k_x, k_y, \omega)$ and $U_-^z(k_x, k_y, \omega)$, respectively). The k_x-k_y distribution at a single frequency (201 kHz) close to the center frequency is displayed in Fig. 6(a–b). As expected, A_0 waves, which have smaller wavelengths and hence larger wavenumbers, form the outer circles. S_0 waves correspond to the inner circles. Based on Fig. 6(a–b), filters using Eq. (7) were designed as shown in Fig. 6(c–d). The filtered FW and BW in k_x-k_y are shown in Fig. 6(e–h). These wavefields were then used to calculate the corresponding single-mode, separated wavefields in the *f-s* domain (i.e., $\overline{U}_{+A_0}^z(x, y, \omega)$, $\overline{U}_{+S_0}^z(x, y, \omega)$, $\overline{U}_{-A_0}^z(x, y, \omega)$, $\overline{U}_{-S_0}^z(x, y, \omega)$) via the 2D IFFT.

4.2.3. RTM imaging using multiple ultrasonic guided-wave modes

The four single-mode pairs at 201 kHz were then used for damage imaging using Eq. (10). The resultant images are shown in Fig. 7.

The mode pairs, including the BW A_0 mode (Fig. 7(a) and (c)), generate a large-value saturated area within the bounds of the damaged region and artifacts outside of the damaged region. However, the A_0-S_0 and S_0-S_0 pairs (Fig. 7(b) and (d), respectively) provide no obviously-useful information. If the employed actuation and reception arrays are identical, based on the reciprocity theory, the A_0-S_0 and S_0-A_0 results would be the same [15].

The results in Fig. 7 used only a single frequency. Similar images were generated at other frequencies as well. In Fig. 8, the stacked, multi-frequency images were generated using Eq. (11) over the frequency range from 183 kHz to 228 kHz, which definite the upper and lower limits of a discrete frequency band, according to the theoretical bandwidth derived for tone-burst signals [55]. Compared with Fig. 7, the stacked images from mode pair A_0-A_0 (Fig. 8(a)) and S_0-A_0 (Fig. 8(c)) show reduced artifacts in the regions outside of the damage region and highlight the damage area more clearly. Nonetheless, the A_0-S_0 (Fig. 8(b)) and S_0-S_0 (Fig. 8(d)) pairs still did not provide beneficial information regarding the half-thickness notch. Dominance of the reflected A_0-related mode pairs (A_0-A_0 and S_0-A_0) is seen when comparing Fig. 8 with Fig. 5 (although Fig. 5 is not a direct combination of the four subplots in Fig. 8). More advanced data fusion techniques might improve image quality as well, e.g., using a weighted sum in Eq. (11) when stacking the results from these four mode pairs. Such improvements were not pursued in this research.

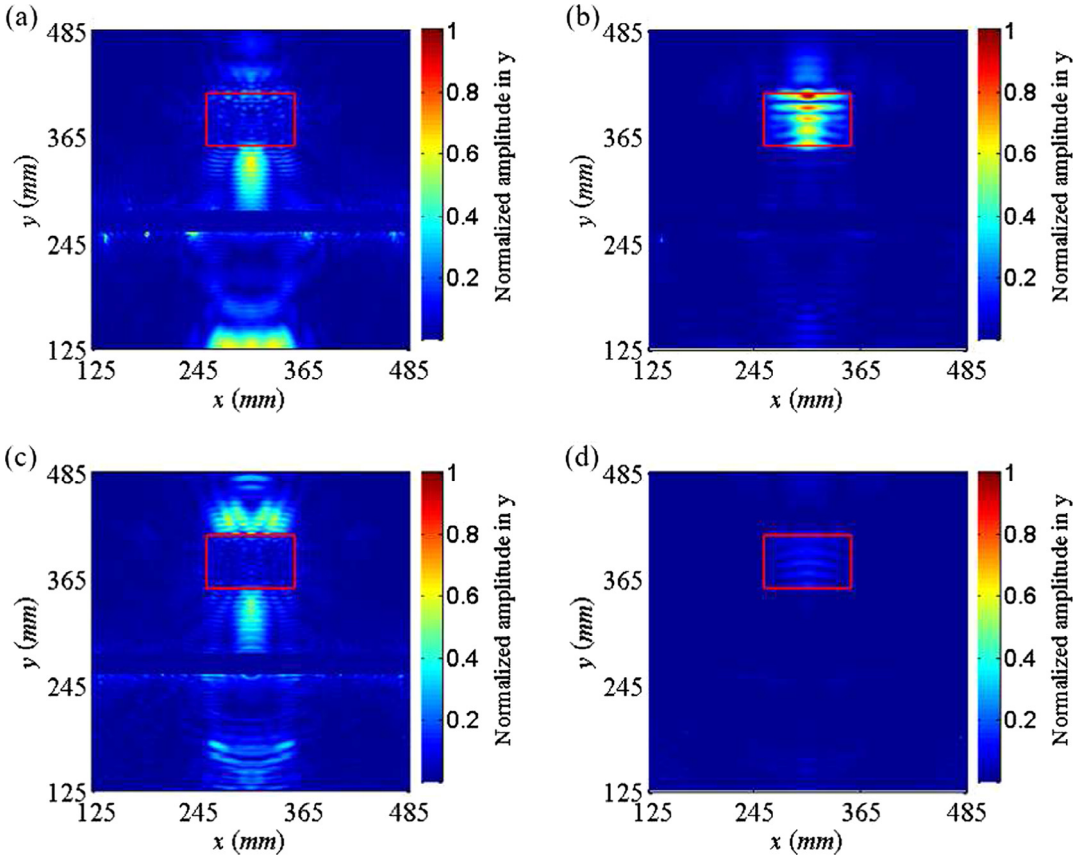

Fig. 15. Stacked multi-mode, *f-k* domain NZLCC for a frequency range of 183–228 kHz using v_y for the MPD (outlined by the red box). Images from mode pairs (a) A_0-A_0, (b) A_0-S_0, (c) S_0-A_0, and (d) S_0-S_0. [Intensity values in the thin, constant-y, rectangular region that covers the array area were set to zero, to mitigate the artifacts caused by the small values of the denominator in Eq. (11) of this region.] (For interpretation of the references to color in this figure legend, the reader is referred to the web version of this article.)

Table 2
Comparison of MPD and HTN images using v_y.

V_y	A_0–A_0	A_0–S_0	S_0–A_0	S_0–S_0
HTN	✔	✔	✔	✖ ✔
MPD	✖	✔	✖	✔

4.3. Imaging results using v_z for the middle-plane disbond

Scattering and mode-conversion behavior is dependent on both wave mode and damage type. Therefore, it is hypothesized that analysis of imaging results from different mode pairs will enable identification of damage type. To study the sensitivity of the proposed techniques to different damage types, a rectangular middle-plane disbond (MPD) was chosen as the second damage case and is shown in Fig. 9. In this subsection, the surface v_z wavefields are employed to generate damage images for this case.

Snapshots of the FW and the BW wavefield at 82.6 μs are shown in Fig. 10, where the damage reflected waves are reconstructed in the BW. Applying the imaging condition from Eq. (3), the total results for the time-domain NZLCC for all wave modes using v_z are obtained and shown in Fig. 11. Compared with the HTN case in Fig. 5, Fig. 11 shows smaller values around the front boundary of the damage and less artifacts.

However, it is very difficult to distinguish what wave modes caused the above differences. Multi-mode wavefield analysis and the proposed imaging algorithms were implemented to provide more information regarding wave modes. Using Eq. (6–8), *f-k* analysis was performed and the resultant k_x-k_y distributions are shown in Fig. 12 at a frequency of 201 kHz, which is similar to Fig. 6(g–h). The A_0 mode back-scattered waves in Fig. 12(a) and in Fig. 6(g) are similar. S_0 back-scattered waves shown in Fig. 6(h) are wider in k_x axis than in Fig. 12(b), which means more energy has been scattered in the x-axis for v_z by the HTN than that by the MPD.

After 2D IFFT of $U_+^z(k_x, k_y, \omega)$ and $U_-^z(k_x, k_y, \omega)$ over a frequency band of 183–228 kHz, the stacked images from the four single-mode pairs using Eq. (11) are shown in Fig. 13. Only $\bar{I}_{\mathrm{NZLCC}}^{zA_0-S_0}(x, y)$ and $\bar{I}_{\mathrm{NZLCC}}^{zS_0-A_0}(x, y)$ (Fig. 13(b) and (d)) appear to provide useful information regarding damage size and location, although these images also contain some artifacts. $\bar{I}_{\mathrm{NZLCC}}^{zS_0-S_0}(x, y)$ shows some low amplitude illumination at the front and back boundaries, although they are difficult to see.

Those artifacts cannot be easily distinguished from the true damaged regions in the images such that coherent reconstruction throughout all mode pairs is difficult to form. From this perspective, the proposed technique is similar to other imaging algorithms, e.g., delay-and-sum (DAS), which can also assume both modes exist and use the two wave speeds of both modes for post-focusing. Despite of this challenge, it is in need to achieve the potential benefits of multi-mode imaging, which include a wider selection of frequencies for improved data acquisition system performance and the ability to simultaneously characterize damage size, location, and type. In addition, the proposed technique using the wave equation-based RTM to provide better imaging results than DAS [56] while also automatically compensate the wave dispersion effects.

4.4. A comparison of imaging results for the HTN and MPD cases using v_z

The performance of stacked multi-frequency, multi-mode NZLCC for both the HTN and MPD cases using v_z are summarized in Table 1 (see

Figs. 8 and 13, respectively, for visual comparison). The "✔" mark indicates that the corresponding image using a mode pair quantifies damage area and provides correct location information, and the "✖" mark means that the image does not provide obviously-useful information regarding damage size or location. The combination of "✔" and "✖" denotes inconclusive results. Although both of the damage types are with the exact same area, the results from each case are drastically different. The reflected S_0 related mode pairs (A_0-S_0 and S_0-S_0) using the wavefields in v_z did not generate quantitative results, likely because the v_z components are not dominant. The next subsection shows the results using wavefields in v_y.

4.5. A comparison of imaging results for the HTN and MPD cases using v_y

By nature, S_0 mode velocities are dominant in the y-direction (i.e., one of the in-plane axes). Procedures similar to those outlined in previous sections were performed using the surface wavefields of v_y for both the HTN and the MPD cases. The multi-mode, stacked images using various mode pairs are shown in Figs. 14 and 15 using Eq. (11). Note that, in these figures, intensity values in a thin, constant-y, rectangular region that covers the array area were set to zero for every subplot. This was done to suppress some large-magnitude artifacts that prohibited viewing of the area of interest. These artifacts may be due to the normalization terms in the denominator of Eq. (11). Relatively small v_y values along the array acted to significantly amplify the noise in that region.

Again, for the HTN case, the A_0-related reflected waves (Fig. 14(a) and (c)) contributed large values in front of and within the damaged region. Compared with the v_z results for HTN (Fig. 8), the v_y-based A_0-S_0 and S_0-S_0 pairs yielded better illumination within the damaged region. For the MPD case, the A_0-A_0 and S_0-A_0 mode pairs still did not provide useful information with wavefields of v_y. However, the S_0-related reflected waves (A_0-S_0 and S_0-S_0) presented quantitative information about the damage location and sizing. A performance evaluation based on the v_y results is summarized in Table 2. The results illustrate sensitivity of damage types to different mode pairs. This suggests that pattern recognition may be useful for identification of damage types in future studies.

5. Conclusions

Using ultrasonic guided waves, a multi-mode damage imaging technique which combines a reverse-time migration algorithm with EFIT, a 3D wave propagation simulator, was proposed in this paper. The time-domain NZLCC imaging condition was used to create compound results from all wave modes. The results represent the damage location and size but do not provide detailed information of different modes. To obtain more information about the contributions from different mode pairs, the proposed method was utilized to separate wave modes. The various wave mode pairs in both the y and z axes behaved differently for the HTN and MPD cases, verifying a damage type sensitivity to different wave modes. Thus, it was concluded that multi-mode imaging has the potential to be used for simultaneous determination of damage type, size and location. Achieving this goal will require further investigation into the interaction of specific mode pairs with various damage types. Additional future work could involve expanding this method to composite applications, for which identifying damage type could be extremely valuable from a SHM or rapid NDE perspective.

The combination of RTM with EFIT is well-suited for modeling complex structures and is easily transferable to other wave propagation simulators as well. Without the limitation of generating single dominant mode waves, wide frequency ranges are accessible, enabling optimal frequencies for a variety of ultrasonic data acquisition systems. High resolution imaging and the flexibility to choose a frequency that is more sensitive to damage types of interest can be achieved.

Acknowledgment

The authors are grateful to Prof. Weidong Zhu for discussing the suitability for using his 3D LDV and kindly offering help. Constructive suggestions were also given by Prof. Paul Sava on multi-mode imaging. The authors acknowledge the support provided by NASA's Convergent Aeronautics Solutions: Digital Twin project (# NNL09AA00A).

Appendix A. Supplementary material

Supplementary data associated with this article can be found, in the online version, at https://doi.org/10.1016/j.ultras.2018.08.005.

References

[1] Y. Cho, J.L. Rose, A boundary element solution for a mode conversion study on the edge reflection of Lamb waves, J. Acoust. Soc. Am. 99 (4) (1996) 2097–2109.
[2] K. Xu, D. Ta, Z. Su, W. Wang, Transmission analysis of ultrasonic Lamb mode conversion in a plate with partial-thickness notch, Ultrasonics 54 (1) (2014) 395–401.
[3] F. Lanza di Scalea, P. Rizzo, A. Marzani, Propagation of ultrasonic guided waves in lap-shear adhesive joints: case of incident A0 Lamb wave, J. Acoust. Soc. Am. 115 (1) (2004) 146–156.
[4] C. Ramadas, K. Balasubramaniam, M. Joshi, C. Krishnamurthy, Interaction of the primary anti-symmetric Lamb mode (A0) with symmetric delaminations: numerical and experimental studies, Smart Mater. Struct. 18 (8) (2009) 085011.
[5] C.M. Yeum, H. Sohn, J.B. Ihn, Lamb wave mode decomposition using concentric ring and circular piezoelectric transducers, Wave Motion 48 (4) (2011) 358–370.
[6] P.Y. Moghadam, N. Quaegebeur, P. Masson, Mode selective generation of guided waves by systematic optimization of the interfacial shear stress profile, Smart Mater. Struct. 24 (1) (2014) 015003.
[7] P. Khalili, P. Cawley, Excitation of single-mode Lamb waves at high-frequency-thickness products, IEEE Trans. Ultrason. Ferroelectr. Freq. Control 63 (2) (2016) 303–312.
[8] H. Chan, B. Masserey, P. Fromme, High frequency guided ultrasonic waves for hidden fatigue crack growth monitoring in multi-layer model aerospace structures, Smart Mater. Struct. 24 (2) (2015) 025037.
[9] V. Giurgiutiu, Tuned Lamb wave excitation and detection with piezoelectric wafer active sensors for structural health monitoring, J. Intell. Mater. Syst. Struct. 16 (4) (2005) 291–305.
[10] H. Gao, J. Rose, Goodness dispersion curves for ultrasonic guided wave based SHM: a sample problem in corrosion monitoring, Aeronaut. J. 114 (1151) (2010) 49–56.
[11] W. Zhou, H. Li, F.G. Yuan, Fundamental understanding of wave generation and reception using d36 type piezoelectric transducers, Ultrasonics 57 (2015) 135–143.
[12] W. Zhou, H. Li, Y. Dong, A. Wang, Sensing properties of optical fiber sensor to ultrasonic guided waves, Smart Struct. Syst. 18 (3) (2016) 471–484.
[13] P. Belanger, P. Cawley, Feasibility of low frequency straight-ray guided wave tomography, NDT & E Int. 42 (2) (2009) 113–119.
[14] W. Zhou, H. Li, F.G. Yuan, Guided wave generation, sensing and damage detection using in-plane shear piezoelectric wafers, Smart Mater. Struct. 23 (1) (2013) 015014.
[15] J. Zhang, B.W. Drinkwater, P.D. Wilcox, A.J. Hunter, Defect detection using ultrasonic arrays: The multi-mode total focusing method, NDT & E Int. 43 (2) (2010) 123–133.
[16] N. Budyn, R. Bevan, A.J. Croxford, J. Zhang, P.D. Wilcox, A. Kashubin, P. Cawley, Sensitivity images for multi-view ultrasonic array inspection, AIP Conference Proceedings, vol. 1949, AIP Publishing, 2018, p. 080001.
[17] L. Le Jeune, S. Robert, E.L. Villaverde, C. Prada, Plane wave imaging for ultrasonic non-destructive testing: Generalization to multimodal imaging, Ultrasonics 64 (2016) 128–138.
[18] E. Iakovleva, S. Chatillon, P. Bredif, S. Mahaut, Multi-mode tfm imaging with artifacts filtering using civa ut forwards models, AIP Conference Proceedings, vol. 1581, AIP, 2014, pp. 72–79.
[19] K. Sy, P. Bredif, E. Iakovleva, O. Roy, D. Lesselier, Development of methods for the analysis of multi-mode tfm images, Journal of Physics: Conference Series, vol. 1017, IOP Publishing, 2018, p. 012005.
[20] A.M. Kamal, B. Lin, V. Giurgiutiu, Exact analytical modeling of power and energy for multimode Lamb waves excited by piezoelectric wafer active sensors, J. Intell. Mater. Syst. Struct. 25 (4) (2014) 452–471.
[21] Z. Chen, L. Fan, Sy Zhang, H. Zhang, Theoretical research on ultrasonic sensors based on high-order Lamb waves, J. Appl. Phys. 115 (20) (2014) 204513.
[22] B. Ren, C.J. Lissenden, PVDF multielement Lamb wave sensor for structural health monitoring, IEEE Trans. Ultrason. Ferroelectr. Freq. Control 63 (1) (2016) 178–185.
[23] C.A. Leckey, M.D. Rogge, C.A. Miller, M.K. Hinders, Multiple-mode Lamb wave scattering simulations using 3D elastodynamic finite integration technique, Ultrasonics 52 (2) (2012) 193–207.
[24] C.A. Leckey, M.D. Rogge, F.R. Parker, Guided waves in anisotropic and quasi-isotropic aerospace composites: Three-dimensional simulation and experiment, Ultrasonics 54 (1) (2014) 385–394.
[25] L. Yu, Z. Tian, C.A. Leckey, Crack imaging and quantification in aluminum plates with guided wave wavenumber analysis methods, Ultrasonics 62 (2015) 203–212.

[26] O. Mesnil, C.A. Leckey, M. Ruzzene, Instantaneous and local wavenumber estimations for damage quantification in composites, Struct. Health Monit. 14 (3) (2015) 193–204.
[27] P. Huthwaite, R. Ribichini, M. Lowe, P. Cawley, D.E. Chimenti, L.J. Bond, D.O. Thompson, Lamb mode selection for accurate wall loss estimation via guided wave tomography, AIP Conference Proceedings, vol. 1581, AIP, 2014, pp. 193–200.
[28] J. Philtron, J. Rose, Mode perturbation method for optimal guided wave mode and frequency selection, Ultrasonics 54 (7) (2014) 1817–1824.
[29] E. Chan, L.F. Rose, C.H. Wang, A comparison and extensions of algorithms for quantitative imaging of laminar damage in plates. II. Non-monopole scattering and noise tolerance, Wave Motion 66 (2016) 220–237.
[30] Z. Hu, W. Lu, M. Thouless, J. Barber, Simulation of wear evolution using fictitious eigenstrains, Tribol. Int. 82 (2015) 191–194.
[31] X. Yu, M. Ratassepp, P. Rajagopal, Z. Fan, Anisotropic effects on ultrasonic guided waves propagation in composite bends, Ultrasonics 72 (2016) 95–105.
[32] P. Zuo, Y. Zhou, Z. Fan, Numerical and experimental investigation of nonlinear ultrasonic Lamb waves at low frequency, Appl. Phys. Lett. 109 (2) (2016) 021902.
[33] P. Zuo, X. Yu, Z. Fan, Numerical modeling of embedded solid waveguides using SAFE-PML approach using a commercially available finite element package, NDT & E Int. 90 (2017) 11–23.
[34] W. Cai, X. Zhou, X. Cui, Optimization of a GPU implementation of multi-dimensional RF pulse design algorithm, Bioinformatics and Biomedical Engineering, (iCBBE) 2011 5th International Conference on, IEEE, 2011, pp. 1–4.
[35] P. Huthwaite, Accelerated finite element elastodynamic simulations using the GPU, J. Comput. Phys. 257 (2014) 687–707.
[36] Y. Luo, Z. Wang, B. Xu, Experimental damage identification in concrete structure using stack migration imaging technology, J. Adv. Concr. Technol. 10 (1) (2012) 41–46.
[37] J. He, F.G. Yuan, A quantitative damage imaging technique based on enhanced CCRTM for composite plates using 2D scan, Smart Mater. Struct. 25 (10) (2016) 105022.
[38] J. Rao, M. Ratassepp, Z. Fan, Guided wave tomography based on full waveform inversion, IEEE Trans. Ultrason. Ferroelectr. Freq. Control 63 (5) (2016) 737–745.
[39] J. Rao, M. Ratassepp, Z. Fan, Limited-view ultrasonic guided wave tomography using an adaptive regularization method, J. Appl. Phys. 120 (19) (2016) 194902.
[40] B. Kaelin, A. Guitton, Imaging condition for reverse time migration, SEG technical program expanded abstracts 2006, Society of Exploration Geophysicists, 2006, pp. 2594–2598.
[41] S. Chattopadhyay, G.A. McMechan, Imaging conditions for prestack reverse-time migration, Geophysics 73 (3) (2008) S81–S89.
[42] L.F. Rose, E. Chan, C.H. Wang, A comparison and extensions of algorithms for quantitative imaging of laminar damage in plates. I. Point spread functions and near field imaging, Wave Motion 58 (2015) 222–243.
[43] R. Zhu, G. Huang, F. Yuan, Fast damage imaging using the time-reversal technique in the frequency–wavenumber domain, Smart Mater. Struct. 22 (7) (2013) 075028.
[44] J. He, F.G. Yuan, Damage identification for composite structures using a cross-correlation reverse-time migration technique, in: The 9th International Workshop on Structural Health Monitoring. Stanford University, IEEE, Stanford, CA, USA, 2013, pp. 98040V–98040V-11, ISBN 978-1-4799-3630-4, https://doi.org/10.1117/12.2218684.
[45] J. He, F.G. Yuan, Lamb-wave-based two-dimensional areal scan damage imaging using reverse-time migration with a normalized zero-lag cross-correlation imaging condition, Struct. Health Monit. (2016) 1475921716674373.
[46] J. He, F.G. Yuan, Damage identification for composite structures using a cross-correlation reverse-time migration technique, Struct. Health Monit. 14 (6) (2015) 558–570.
[47] A. Volker, L. Pahlavan, G. Blacquiere, D.E. Chimenti, L.J. Bond, Crack depth profiling using guided wave angle dependent reflectivity, AIP Conference Proceedings, vol. 1650, AIP, 2015, pp. 785–791.
[48] M. Ruzzene, Frequency–wavenumber domain filtering for improved damage visualization, Smart Mater. Struct. 16 (6) (2007) 2116.
[49] Z. Tian, L. Yu, Lamb wave frequency–wavenumber analysis and decomposition, J. Intell. Mater. Syst. Struct. 25 (9) (2014) 1107–1123.
[50] P. Huthwaite, F. Simonetti, High-resolution guided wave tomography, Wave Motion 50 (5) (2013) 979–993.
[51] P. Fellinger, R. Marklein, K. Langenberg, S. Klaholz, Numerical modeling of elastic wave propagation and scattering with EFIT - elastodynamic finite integration technique, Wave Motion 21 (1) (1995) 47–66.
[52] M.D. Rogge, C.A. Leckey, Characterization of impact damage in composite laminates using guided wavefield imaging and local wavenumber domain analysis, Ultrasonics 53 (7) (2013) 1217–1226.
[53] G.B. Santoni, L. Yu, B. Xu, V. Giurgiutiu, Lamb wave-mode tuning of piezoelectric wafer active sensors for structural health monitoring, J. Vib. Acoust. 129 (6) (2007) 752–762.
[54] Ł Ambroziński, T. Stepinski, T. Uhl, Efficient tool for designing 2D phased arrays in Lamb waves imaging of isotropic structures, J. Intell. Mater. Syst. Struct. 26 (17) (2015) 2283–2294.
[55] J. He, Time-reversal Based Array Damage Imaging in Structural Health Monitoring, North Carolina State University, 2015.
[56] G.T. Schuster, Reverse-time migration generalized diffraction stack migration, SEG Technical Program Expanded Abstracts 2002, Society of Exploration Geophysicists, 2002, pp. 1280–1283.